Study of the influence of dopants on the crystalline perfection of ferroelectric glycine phosphite single crystals using high-resolution X-ray diffraction analysis

Krishnamurthy Senthil Kumar,[a] Sridharan Moorthy Babu[a]* and G. Bhagavannarayana[b]

[a]Crystal Growth Centre, Anna University, Chennai 600025, India, and [b]Crystal Growth and X-ray Analysis, National Physical Laboratory (CSIR), New Delhi 110012, India. Correspondence e-mail: smoorthybabu@yahoo.com

Good quality and optically transparent single crystals of pure and doped glycine phosphite (GPI) were grown by both solvent-evaporation and temperature-cooling techniques. Dopants were chosen in different categories, namely transition metals (Cr, Mn, Co, Ni, Zn, Mg, Cd), rare-earth metals (Ce, Nd, La), dyes (rhodamine B, malachite green, fluorescein) and an amino acid (L-proline). The concentration of dopants was chosen depending on the category of dopants and the quality of crystallization during the growth process. The crystalline perfection of the as-grown pure and doped GPI crystals was investigated by high-resolution X-ray diffraction at room temperature. A multicrystal X-ray diffractometer employing a well collimated and highly monochromated Mo $K\alpha_1$ beam and set in the $(+, -, -, +)$ configuration was employed. Most of the crystal specimens show excellent crystalline perfection. However, grain boundaries, low-angle tilt boundaries, and vacancy and interstitial point defects were observed in some crystal specimens.

1. Introduction

Ferroelectricity in glycine phosphite single crystals (hydrogen-bonded compounds), abbreviated as GPI, was first observed in 1996 (Dacko et al., 1996). GPI and deuterated GPI undergo a continuous ferroelectric phase transition at 224 and 324 K, respectively. Both these crystals are of the order–disorder type of second-order ferroelectric phase transition. They belong to the monoclinic system with space group $P2_1/a$ in the paraelectric phase and $P2_1$ in the ferroelectric phase (Baran et al., 2002; Lapsa et al., 2000) and are characterized by the linking of hydrogen bonds of the inorganic HPO_3^- tetrahedra to zigzag chains, each glycine molecule being attached via OH···O bonds to these inorganic units. The cell parameters of GPI are $a = 7.401$ (3), $b = 8.465$ (3), $c = 9.737$ (3) Å, $\alpha = \gamma = 90$, $\beta = 100.73°$ and $V = 599.4$ (4) Å^3 (Lapsin et al., 2005). The growth of large-size bulk crystals of pure GPI has been reported recently (Perumal et al., 2010). To realize the full efficiency of a ferroelectric device, the constituent crystals should be free from defects (Bhagavannarayana, Budakoti et al., 2005). High-resolution X-ray diffraction (HRXRD) is one of the most widely used techniques for determining crystalline perfection and for defect studies in single crystals. Evaluation of crystalline perfection is very important, particularly when the crystals are doped, as these dopants influence the crystalline perfection; this is especially true at higher concentrations and for larger-sized crystals (Bhagavannarayana et al., 2008). The present investigation includes the growth of different categories of doped GPI single crystals and their characterization for crystalline perfection using HRXRD analyses.

2. Experimental

2.1. Crystal growth

Pure GPI was synthesized by dissolving an equimolar ratio of glycine (NH_2CH_2COOH; Merk) and *ortho*-phosphorous acid (H_3PO_3; Sigma Aldrich) with millipore water as the solvent. The synthesized material was subjected to repeated recrystallization for purification. The synthesized GPI material was doped with various categories of dopants, namely transition metals (with a concentration of 1 mol% of Cr^{3+}, Mn^{2+}, Co^{2+} and Ni^{2+}, and 10 mol% of Zn^{2+}, Mg^{2+} and Cd^{2+} in the form of nitrates and chlorides), rare-earth metals (0.2 mol% of Ce^{3+} and Nd^{3+}, and 1 mol% of La^{3+}), dyes (1 mol% of rhodamine B, 0.5 mol% of malachite green and 0.2 mol% of fluorescein) and an amino acid (3 mol% of L-proline). Dopant ions are distributed homogeneously in the grown crystals. Pure and doped GPI crystals were grown by solvent-evaporation as well as temperature-lowering methods. Optically polished *b*-axis-oriented seed crystals were used for the growth of bulk crystals. During bulk crystal growth, a supersaturated solution was prepared at 318 K and placed in a constant-temperature bath with an accuracy of 0.01 K. Initi-

ally, the cooling rate was maintained at 0.1 K d^{-1} for a week, and then it was increased to 0.2 K d^{-1} until the end of the growth period. Bulk crystals of pure and doped GPI were obtained in 30 d. The crystals were found to be nonhygroscopic.

2.2. High-resolution X-ray diffraction characterization

The crystalline perfection of the grown single crystals was analyzed by HRXRD by employing a multicrystal X-ray diffractometer developed at the National Physical Laboratory (NPL), New Delhi (Lal & Bhagavannarayana, 1989). The divergence of the X-ray beam emerging from a fine-focus X-ray tube (Philips X-ray Generator; 0.4 × 8 mm; 2 kW Mo) is first reduced by a long collimator fitted with a pair of fine-slit assemblies. The foreshortening angle of the beam emerging from the target was kept at 3° instead of the usual value of 6°, though the intensity is expected to be less in view of having better resolution. An Mo target was chosen instead of the commonly used Cu as the wavelength of Mo $K\alpha_1$ (0.70926) is less than half of that of Cu $K\alpha_1$ (1.54056 Å) and hence the expected resolution for HRXRD experiments is better. (However, owing to the larger wavelength of Cu $K\alpha_1$ the workable angular range is greater and hence more convenient in some cases, such as in powder XRD).

This collimated beam is diffracted twice by two Bonse–Hart-type (Bonse & Hart, 1965) monochromator crystals, and thus the diffracted beam contains well resolved Mo $K\alpha_1$ and Mo $K\alpha_2$ components. The Mo $K\alpha_1$ beam is isolated with the help of a fine-slit arrangement and allowed to further diffract from an independent third Si monochromator crystal set in dispersive geometry, (+, −, −). All three Si(111) monochromator crystals are plane crystals and are set for diffraction from the (111) planes in the symmetrical Bragg geometry. The specimen crystal was aligned in the (+, −, −, +) configuration, wherein the specimen crystal is in nondispersive geometry with respect to the third monochromator. Owing to the dispersive configuration of the third monochromator crystal with respect to the second monochromator, the spectral quality of the diffracted beam emerging from the third monochromator is high ($\Delta\lambda/\lambda \simeq 10^{-5}$; horizontal divergence $\gg 3''$) and hence, though the lattice constant of the monochromator crystal and the specimen are different, the unwanted experimental dispersion broadening in the diffraction curve of the specimen crystal [ΔFWHM = $\Delta\lambda/\lambda(\tan\theta_M - \tan\theta_S)$, θ_M and θ_S being the Bragg diffraction angles of the monochromator and the specimen crystals] is insignificant. The advantage of the dispersive configuration (+, −, −) of monochromators over the nondispersive configuration (+, −, +) has been discussed in a recent article (Bhagavannarayana & Kushwaha, 2010). It may be mentioned here that, as the third monochromator stage is independent and placed at a large distance of around 75 cm from the Bonse–Hart crystals, the unwanted divergent Mo $K\alpha_1$ and scattered radiation (though most of this is stopped by the slit assembly after the second monochromator) from the tails of the first and second monochromators are eliminated to a great extent.

The specimen can be rotated about the vertical axis, which is perpendicular to the plane of diffraction, with a minimum angular interval of 0.4″. The diffraction or rocking curves (RCs) were recorded by changing the glancing angle (angle between the incident X-ray beam and the surface of the specimen) around the Bragg diffraction peak position (taken as zero for the sake of convenience) starting from a suitable arbitrary glancing angle and ending at a glancing angle after the peak so that all the meaningful scattering intensities on both sides of the peak are included in the diffraction curve. The RCs were recorded using the so-called ω-scan technique, wherein the detector was kept at a fixed angular position $2\theta_B$ (θ_B being the Bragg diffraction angle) with a wide opening for its slit. The slit width was kept at around 1 mm, through which an intensity distribution for an angular range of up to around 500″ on both sides of the 2θ position (of the detector, which was at a distance of around 165 mm from the sample) can be received, which could cover all the peaks due to various grain boundaries or the meaningful scattering intensity for the specimens studied in the present investigation. It may be mentioned here that, when the residual direct beam that may emerge through the crystal is stopped, even if the slit width is much greater than 1 mm, the observed RC along with the scattering intensity along the tails of the RC does not change. The voltage and current set for the X-ray source are 50 kVA and 30 mA, respectively. The size of the X-ray beam impinging on the surface is 5 × 0.2 mm with a stable beam intensity of ∼6.2 × 10^3 counts s^{-1}. The beam was allowed to fall at the center of the parallel plate-shaped specimen during the experiments. However, before choosing the central region, the homogeneity of the crystalline perfection was confirmed by recording the RCs across the sample at different places.

The ω-scan method is highly appropriate for recording the short-range-order scattering caused by defects, by the scattering from local Bragg diffractions from agglomerated point defects, or by low-angle and very low angle structural grain boundaries (Bhagavannarayana & Kushwaha, 2010). In the case of 2θ–θ or 2θ–ω scans, the experimentally obtained RC contains information about a single grain, for which we align the scan. The rocking curve is thus expected to be very sharp, as the narrow-slit detector will not receive diffracted intensities from the other grains, which are misoriented with respect to the grain under investigation (*i.e.* aligned for diffraction), or the diffuse scattering from point defects and their aggregates. Conversely, in the relatively simple ω scan, with a sufficiently wide slit for the detector, if the crystal contains structural grain boundaries, we get all the peaks in the RC. On the other hand, in an ω scan, if we obtain a single sharp peak it confirms that the specimen crystal has a single domain with a single orientation. It is worth mentioning here that, unless the exploring beam is very narrow (say $\Delta\lambda/\lambda \simeq 10^{-5}$ and horizontal divergence $\ll 3''$), the RCs obtained from ω scans do not yield resolved peaks for a crystal that contains grain boundaries, except for a very broad peak though the crystal. Using the in-house-developed diffractometer, we have observed the splitting of rocking curves recorded *via* an ω scan in a variety of crystals, including LiNbO$_3$ (Bhagavannarayana, Anantha-

murthy *et al.*, 2005), Bi$_4$Ge$_3$O$_{12}$ (Choubey *et al.*, 2002), oxalic acid-doped ammonium dihydrogen phosphate (Bhagavannarayana *et al.*, 2008), L-threonine-doped potassium dihydrogen phosphate (KDP) (Kushwaha *et al.*, 2010), urea-doped tristhioureazinc(II) sulfate (Bhagavannarayana & Kushwaha, 2010) and LiF (Bhagavannarayana, Kushwaha *et al.*, 2011), and have demonstrated with the help of section topographs that these are due to very low (tilt angle $\alpha \leq 1''$) and low-angle ($\alpha > 1''$ but less than a degree) structural grains. With the help of powder XRD, it was also confirmed that this type of minute splitting in the RC is not due to different phases, even in the doped crystals (Bhagavannarayana *et al.*, 2008; Kushwaha *et al.*, 2010; Bhagavannarayana & Kushwaha, 2010). As shall be seen in §3 [equation (2)], the theoretical FWHM is nearly proportional to the wavelength of the exploring X-ray beam and hence for the purpose of obtaining resolved peaks due to different structural grains of the specimen crystal, Mo $K\alpha_1$ is better than Cu $K\alpha_1$. It was in view of these advantages, and the various types of crystals studied in the present investigation, that the ω-scan technique using Mo $K\alpha_1$ radiation was adopted.

Before recording the diffraction curve, the specimen was first lapped and chemically etched in a nonpreferential etchant of water and acetone mixed in a 1:2 volume ratio, to remove the noncrystallized solute atoms remaining on the surface of the crystal and the layers that may sometimes form on the surfaces of crystals grown by solution methods (Bhagavannarayana, Ananthamurthy *et al.*, 2005) and to ensure the surface planarity.
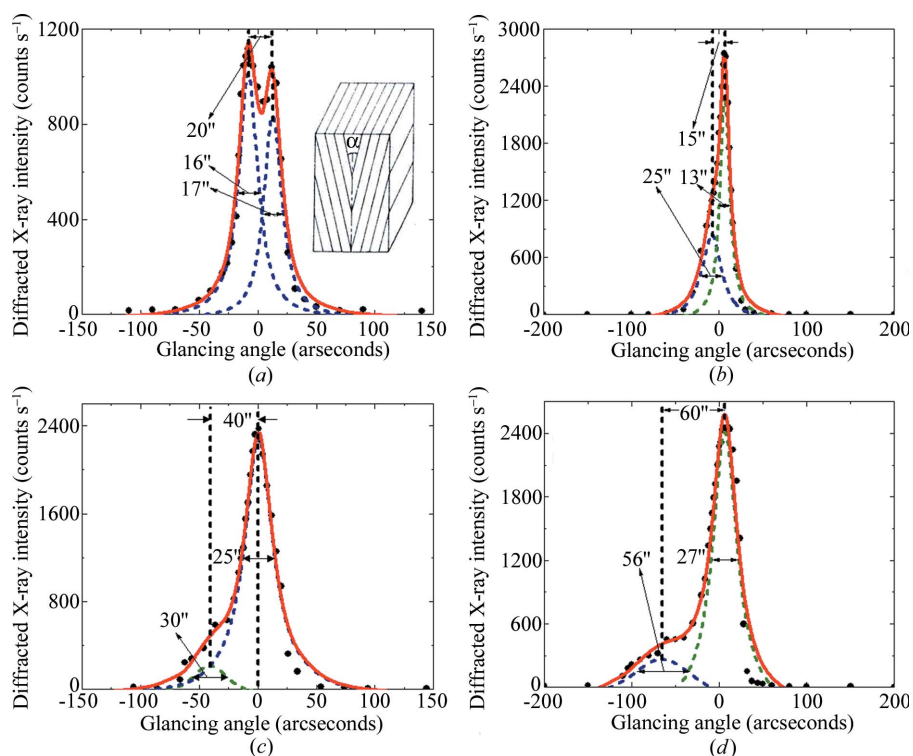
3. Results and discussion

In the present study, HRXRD analysis was carried out for as-grown pure and doped GPI single crystals of dimension $\sim 8 \times 6 \times 2$ mm. The HRXRD results can be classified into five different types.

Fig. 1 shows the HRXRD RCs recorded for typical pure and for Zn-, malachite green- and rhodamine B-doped GPI single-crystal specimens. The solid line (convoluted curve) is a good fit to the experimental points represented by the filled circles. On deconvolution of the diffraction curve, it was clear that the curves contain additional peaks, which are 20, 15, 40 and 60$''$ away from the main peak for pure and for Zn-, malachite green- and rhodamine B-doped GPI crystals, respectively. These additional peaks depict an internal very low angle structural boundary. For a better understanding, a schematic of a structural grain boundary is given in the inset of Fig. 1(*a*) for pure GPI. The inset shows that the two regions of the crystal are misoriented by a finite angle α, also known as the tilt angle (misorientation angle between the two crystalline regions on both sides of the structural grain boundary), and the two regions may be perfect. If the value of α is $\leq 1'$, one may call it a very low angle boundary. If $\alpha > 1'$ but less than a degree, one may call it a low-angle boundary. More details of such structural grain boundaries, including their effect on physical properties, are available elsewhere (Bhagavannarayana & Kushwaha, 2010; Bhagavannarayana, Ananthamurthy *et al.*, 2005). The angular separation between the two peaks gives the tilt angle α, *i.e.* 20, 15, 40 and 60$''$ for pure and for Zn-, malachite green- and rhodamine B-doped GPI crystals, respectively, for the specimens depicted in Fig. 1. The FWHMs of the main peak and the very low angle boundary are, respectively, 16 and 17$''$ for pure GPI, 25 and 13$''$ for Zn-GPI, 30 and 25$''$ for malachite green-GPI, and 56 and 27$''$ for rhodamine B-GPI crystals, as shown in Fig. 1. These low values reveal the fact that both the regions of the crystal are nearly perfect as one can expect such low values only for crystals with reasonable quality. Though the specimens contain a very low angle boundary, the relatively low angular spread of around 200$''$ of the diffraction curve and the low FWHM values show that the crystalline perfection is reasonably good. Thermal fluctuations or mechanical disturbances during the growth process could be responsible for the observed very low angle boundary. It may be mentioned here that such very low angle boundaries (which are unlikely to degrade the properties) could be detected with well resolved peaks in the diffraction curves only because of the high resolution of the diffractometer, characterized by very low values of

Figure 1
High-resolution X-ray diffraction curves of (*a*) pure GPI crystals and crystals doped with (*b*) Zn, (*c*) malachite green and (*d*) rhodamine B.

wavelength spread (*i.e.* $\Delta\lambda/\lambda$) and horizontal divergence for the exploring or incident beam (respectively, around 10^{-5} and much less than 3″).

Fig. 2 shows the RCs recorded for crystal specimens doped with 0.2 mol% of Ce and Nd, 1 mol% of Mn, Co and Ni, 3 mol% of L-proline, and 10 mol% of Mg. The RCs were quite sharp without any of the satellite peaks that may be observed either because of internal structural grain boundaries (Bhagavannarayana, Ananthamurthy *et al.*, 2005), as seen in Fig. 1, or because of epitaxial layers which may sometimes form in crystals grown from solution (Bhagavannarayana *et al.*, 2006). The FWHMs of the RCs were 9″ for Ce- and Co-doped GPI, and 8, 14, 7.5, 11 and 10″ for Nd-, Ni-, L-proline-, Mn- and Mg-doped GPI crystals, which were very close to the value expected from the plane wave theory of dynamical X-ray diffraction (Batterman & Cole, 1964). The FWHM

($\Delta\theta_{1/2}$) of such a theoretical curve can be readily obtained from the following simplified equation:

$$\Delta\theta_{1/2} = \frac{2\tau}{\sin 2\theta_B} F'_H |P|, \tag{1}$$

where $\tau = r_e \lambda^2 / \pi V$, r_e is the classical electron radius, V is the volume of the unit cell, P is the polarization factor and F'_H is the real part of the structure factor for the hkl reflection. The above equation may be further simplified as

$$\Delta\theta_{1/2} = \frac{2\lambda d r_e}{\pi V \left[1 - (\lambda/2d)^2\right]^{1/2}} F'_H |P|, \tag{2}$$

in which the Bragg angle θ_B is replaced by the lattice spacing d of the diffracting planes. As a first approximation, as seen in equation (2), the FWHM is directly proportional to the wavelength of the X-ray beam as the factor $(\lambda/2d)^2$ in the denominator is always less than one for all practical λ and d values. More details, including the details for obtaining a theoretical RC, are given in a recent article (Bhagavannarayana, Kushwaha *et al.*, 2011). The theoretical curve obtained for a GPI crystal using the (120) planes and having a FWHM value of 0.11″ is given in Fig. 2(*h*). This very low
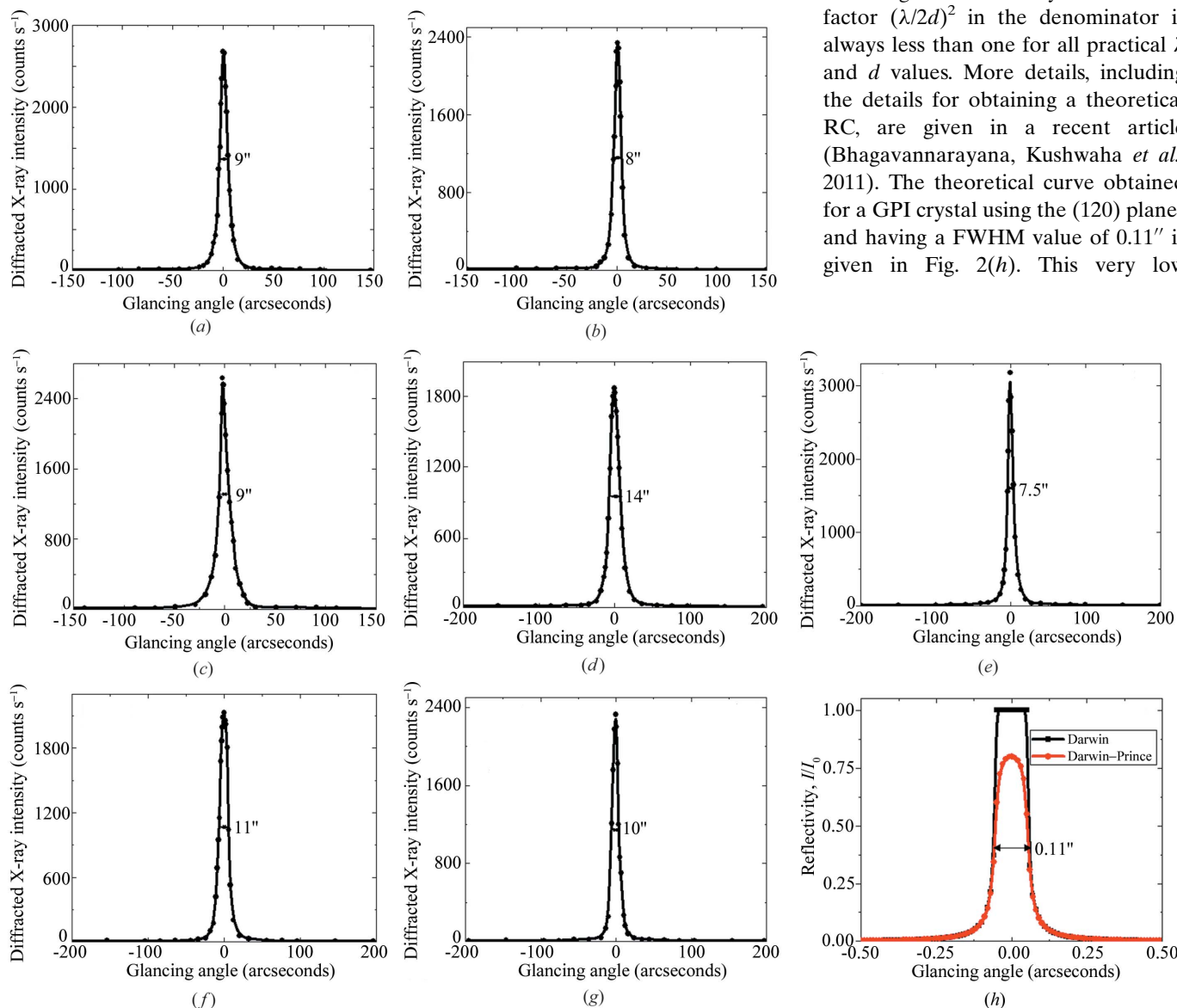
Figure 2
High-resolution X-ray diffraction curves of GPI crystals doped with (*a*) Ce, (*b*) Nd, (*c*) Co, (*d*) Ni, (*e*) L-proline, (*f*) Mn and (*g*) Mg, and (*h*) theoretical diffraction curves for a pure GPI single crystal.
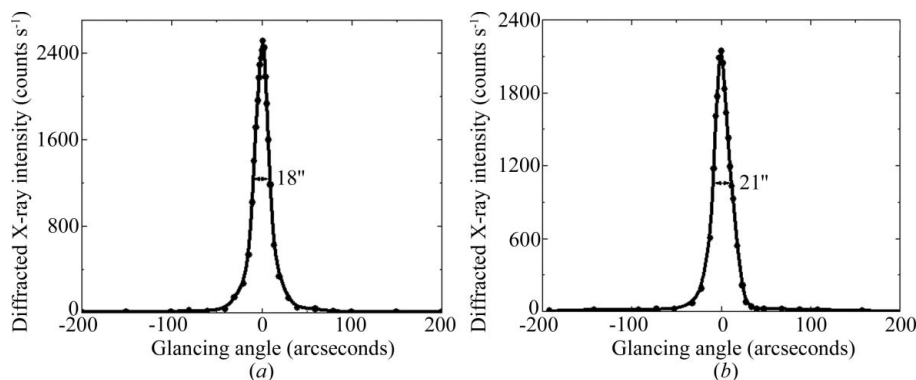
Figure 3
High-resolution X-ray diffraction curves of (a) La- and (b) Cd-doped GPI crystals.

FWHM value for the RC (compared with, for example, a value of ~9.5″ for CdTe) is expected because of the light elements (the lower the atomic number, the lower the atomic scattering factor) present in the GPI crystal. Fig. 2(h) in fact contains two diffraction curves: one the so-called Darwin, where the phenomenon of linear absorption of X-rays is not taken into consideration, and the other the well known Darwin–Prince curve, in which the absorption correction is taken into account. From the Darwin–Prince curve, it is observed that the reflectivity at the peak of the diffraction maximum is reduced considerably, in contrast to LiF (Bhagavannarayana, Kushwaha et al., 2011), owing to the absorption of X-rays in GPI. The departure from the ideal state of atomic arrangement in the specimen will be seen as the difference between the half widths. Of course, the experimental arrangement for recording diffraction curves should be such that the exploring X-ray beams are nearly parallel and monochromatic. The lowest experimentally observed FWHM so far obtained with the present diffractometer is 2.7″ for an excellent quality KDP single crystal (Dhanaraj et al., 2009), with which one can realize the resolution of the diffractometer. The single sharp diffraction curves with very low FWHMs obtained for the doped GPI crystals indicate that the crystalline perfection was quite good. The crystal specimens are nearly perfect single crystals without any internal structural grain boundaries.

Fig. 3 shows the RCs recorded for typical solution-grown GPI crystals doped with 1 mol% of La and 10 mol% of Cd. The curves contain a single peak and indicate that the specimens are free from structural grain boundaries. The FWHMs of the curves were 18 and 21″ for the La- and Cd-doped GPI crystals. These FWHM values are somewhat higher than that expected from the plane wave theory of dynamical X-ray diffraction (Batterman & Cole, 1964) for an ideally perfect crystal but close to that expected for nearly perfect real crystals. This broadness with good scattering intensity along the wings of the diffraction curves on both sides of the peak indicates that the crystals contain both vacancy and interstitial types of defects. Such defects are very commonly observed in almost all real crystals, including crystals formed by natural geological processes, and are often unavoidable because of thermodynamical conditions. It is worth mentioning here that the observed scattering due to point defects is of short-range

order, as the strain caused by such minute defects is limited to the defect core and long-range order could not be expected. Hence one cannot observe any change in the lattice parameters.
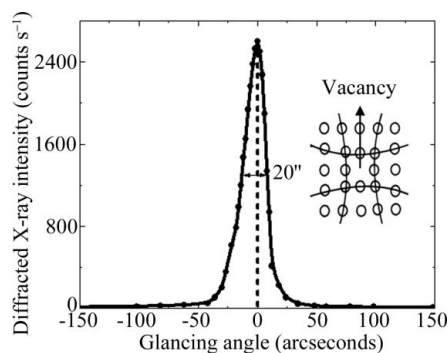
Fig. 4 shows the high-resolution X-ray diffraction curve recorded for a 1 mol% Cr-doped GPI crystal specimen. The solid line (convoluted curve) is a good fit to the experimental points represented by the filled circles. On deconvolution of the diffraction curve, it is clear that the curve contains two additional peaks, which are 22 and 64″ away from the main peak (with maximum intensity). These two additional peaks correspond to two internal structural very low angle ($\alpha \leq 1'$) boundaries whose tilt angles are 42 and 22″ from their adjoining regions. The FWHMs of the main peak and the very low angle boundaries are, respectively, 21, 40 and 58″. Though the specimen contains very low angle boundaries, the relatively low angular spread of around 200″ of the diffraction curve and the low FWHM values show that the crystalline perfection is reasonably good. The affect of such very low angle boundaries may not be very significant in many device applications. However, for applications related to anisotropic properties like piezoelectricity (Bhagavannarayana, Budakoti et al., 2005) and phase matching (for nonlinear optical crystals; Bhagavannarayana, Riscob & Shakir, 2011), it is better to know the tilt angles quantitatively to decide whether such crystals can be used for these applications. Thermal fluctuations, mechanical disturbances or segregation of solvent molecules during the growth process could be responsible for the observed very low angle boundaries.

Fig. 5 shows the RC recorded for a typical 0.2 mol% fluorescein-doped single-crystal specimen. As seen in the figure, the RC contains a single sharp peak and indicates that the specimen is free from structural grain boundaries. The FWHM of the curve is 20″, which is somewhat higher than that expected from the plane wave theory of dynamical X-ray diffraction for an ideally perfect crystal. The broadening of the rocking curve without the presence of any splitting can be
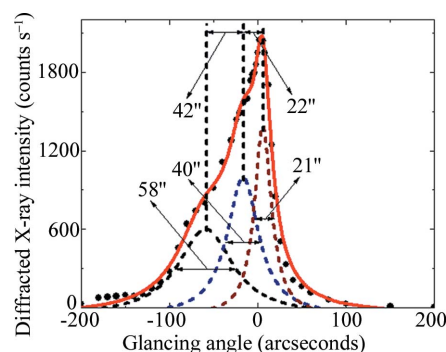
Figure 4
High-resolution X-ray diffraction curve of Cr-doped GPI crystals.

Figure 5
High-resolution X-ray diffraction curve of fluorescein-doped GPI crystals.

attributed to a variety of defects, such as randomly oriented mosaic blocks, dislocations, Frankel defects, implantation-induced defects (due to the simultaneous existence of vacancies and interstitial defects) *etc*. However, depending upon the nature of the asymmetry, as investigated in our previous articles, one can expect predominant occupation of vacancy or interstitial defects (Lal & Bhagavannarayana, 1989; Bhagavannarayana, Choubey *et al.*, 2005; Bhagavannarayana *et al.*, 2008, 2010; Bhagavannarayana, Kushwaha *et al.*, 2011; Kushwaha *et al.*, 2010; Bhagavannarayana & Kushwaha, 2010), which can be realized in the following way. For a particular angular deviation ($\Delta\theta$) of glancing angle with respect to the peak position, the scattering intensity is much higher in the negative direction than in the positive direction. This feature clearly indicates that the crystal contains predominantly vacancy-type defects rather than interstitial defects. These vacancy defects may be present as a result of fast growth (Bhagavannarayana *et al.*, 2010). As shown schematically in the inset of Fig. 5, the lattice around these defects undergoes tensile stress and the lattice parameter *d* (interplanar spacing) increases. This leads to more scattering (also known as diffuse X-ray scattering) intensity at slightly lower Bragg angles (θ_B) as *d* and $\sin\theta_B$ are inversely proportional to each other in the Bragg equation ($2d\sin\theta_B = n\lambda$, *n* and λ being the order of reflection and wavelength, respectively, which are fixed). However, if these point defects are present with very low density, as in the present case, they have hardly any affect on the performance of the devices based on such crystals. More details may be obtained from the study of high-resolution diffuse X-ray scattering measurements (Bhagavannarayana, Ananthamurthy *et al.*, 2005). If the concentration is high, the FWHM would be much higher and would often lead to structural grain boundaries (Bhagavannarayana *et al.*, 2008). Point defects to some extent are unavoidable owing to thermodynamical considerations and growth conditions (Bhagavannarayana *et al.*, 2010).

4. Conclusions

Pure and doped GPI single crystals were grown by the low-temperature solution-growth method. HRXRD analysis of pure and of Zn-, malachite green- and rhodamine B-doped GPI single crystals reveals that the crystals contain an internal

very low angle structural boundary, which may be due to thermal fluctuations or mechanical disturbances during the growth process. HRXRD analysis of Ce-, Co-, Nd-, Ni-, L-proline-, Mn- and Mg-doped GPI crystals indicates that the crystalline perfection is extremely good, since the FWHMs of the above crystals are in the range 7.5–14″ (which values are comparable to those predicted by the plane wave theory of dynamical X-ray diffraction), and the crystals are without any internal structural grain boundaries. HRXRD analysis of La- and Cd-doped GPI crystals shows that the crystalline perfection is reasonably good and the crystals are free from structural grain boundaries but contain both vacancy and interstitial types of point defects. HRXRD analysis of a Cr-doped GPI crystal reveals that the crystal contains very low angle boundaries, which may be due to inhomogeneous segregation of the Cr atom in the pure GPI crystalline matrix. HRXRD analysis of fluorescein-doped GPI crystals indicates that the crystal contains predominantly vacancy-type defects rather than interstitial defects, which may be a result of fast growth.

References

Baran, J., Lukaszewicz, K., Pietraszko, A. & Sleɗz, M. (2002). *J. Mol. Struct.* **611**, 155–168.
Batterman, B. W. & Cole, H. (1964). *Rev. Mod. Phys.* **36**, 681–717.
Bhagavannarayana, G., Ananthamurthy, R. V., Budakoti, G. C., Kumar, B. & Bartwal, K. S. (2005). *J. Appl. Cryst.* **38**, 768–771.
Bhagavannarayana, G., Budakoti, G. C., Maurya, K. K. & Kumar, B. (2005). *J. Cryst. Growth*, **282**, 394–401.
Bhagavannarayana, G., Choubey, A., Shubin, Yu. V. & Lal, K. (2005). *J. Appl. Cryst.* **38**, 448–454.
Bhagavannarayana, G. & Kushwaha, S. K. (2010). *J. Appl. Cryst.* **43**, 154–162.
Bhagavannarayana, G., Kushwaha, S. K., Shakir, Mohd. & Maurya, K. K. (2011). *J. Appl. Cryst.* **44**, 122–128.
Bhagavannarayana, G., Parthiban, S. & Meenakshisundaram, S. (2006). *J. Appl. Cryst.* **39**, 784–790.
Bhagavannarayana, G., Parthiban, S. & Meenakshisundaram, S. (2008). *Cryst. Growth Des.* **8**, 446–451.
Bhagavannarayana, G., Rajesh, P. & Ramasamy, P. (2010). *J. Appl. Cryst.* **43**, 1372–1376.
Bhagavannarayana, G., Riscob, B. & Shakir, Mohd. (2011). *Mater. Chem. Phys.* **126**, 20–23.
Bonse, U. & Hart, M. (1965). *Appl. Phys. Lett.* **7**, 238–240.
Choubey, A., Bhagavannarayana, G., Shubin, Yu. V., Chakraborty, B. R. & Lal, K. (2002). *Z. Kristallogr.* **217**, 515–521.
Dacko, S., Czapla, Z., Baran, J. & Drozd, M. (1996). *Phys. Lett. A*, **223**, 217–220.
Dhanaraj, P. V., Rajesh, N. P., Mahadevan, C. K. & Bhagavannarayana, G. (2009). *Physica B*, **404**, 2503–2508.
Lal, K. & Bhagavannarayana, G. (1989). *J. Appl. Cryst.* **22**, 209–215.
Kushwaha, S. K., Shakir, Mohd., Maurya, K. K., Shah, A. L., Wahab, M. A. & Bhagavannarayana, G. (2010). *J. Appl. Phys.* **108**, 033506.
Lapsa, K., Drozdowski, M., Ziobrowski, P. & Szczepanska, L. (2000). *Ferroelectrics*, **239**, 87–92.
Lapsin, A. E., Smolin, Yu. I. & Pankova, G. A. (2005). *J. Struct. Chem.* **46**, 315–319.
Perumal, R., Senthil Kumar, K., Moorthy Babu, S. & Bhagavannarayana, G. (2010). *J. Alloys Compd.* **490**, 342–349.